

# Solvation at metal/water interfaces: An ab initio molecular dynamics benchmark of common computational approaches

**Heenen, Hendrik H.; Gauthier, Joseph A.; Kristoffersen, Henrik H.; Ludwig, Thomas ; Chan, Karen**

*Published in:*
Journal of Chemical Physics

*Link to article, DOI:*
10.1063/1.5144912

*Publication date:*
2020

*Document Version*
Peer reviewed version

# Supporting Information – Solvation at metal/water interfaces: An ab initio molecular dynamics benchmark of common computational approaches

Hendrik H. Heenen,[†] Josef A. Gauthier,[‡] Henrik H. Kristofferson,[†] Thomas Ludwig,[‡] and Karen Chan[*,†]

†*Department of Physics, Technical University of Denmark, DK-2800, Kgs. Lyngby, Denmark*

‡*SUNCAT Center for Interface Science and Catalysis, Department of Chemical Engineering, Stanford University, Stanford, California 94305, United States*

¶*SUNCAT Center for Interface Science and Catalysis, SLAC National Accelerator Laboratory, 2575 Sand Hill Road, Menlo Park, California 94025, United States*

E-mail: kchan@fysik.dtu.dk

# I Convergence of *ab initio* Molecular Dynamics

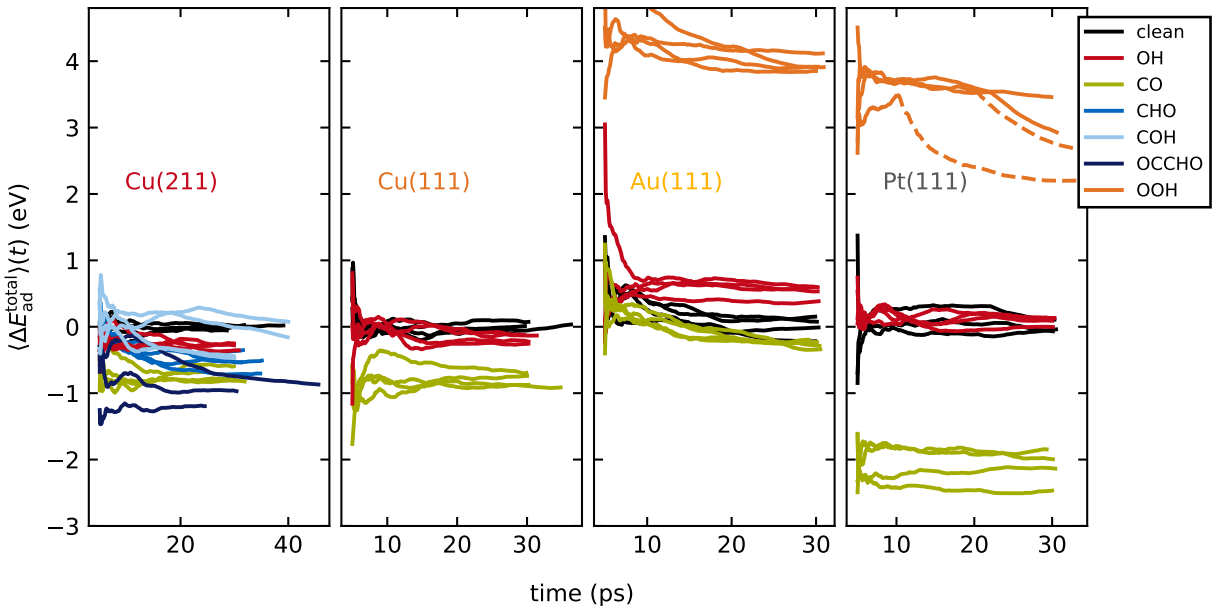


Figure S1: Total average adsorption energy (eq. 1 main text) against simulation time $\langle \Delta E_{\mathrm{ad}}^{\mathrm{total}} \rangle (t)$ (cumulative average) after the equilibration period of 5 ps for all individual trajectories. The energies are of the uncorrected trajectories including chemical reactions (see main text), the dashed lines for OOH on Pt(111) represent energies where the DFT metal slab artefact is present (see Sec. VIIIa). The gas phase references are constant for all time steps.

Table S1: Total average adsorption energy (eq. 1 main text) $\langle \Delta E_{\mathrm{ad}}^{\mathrm{total}} \rangle(t)$ and drift in total energy $\frac{dE^{\mathrm{total}}}{dt}$ (meV/ps) for the four individual trajectories of each system after 5 ps equilibration and at least 25 ps sampling time. Data for the OOH/Pt(111) is corrected for occurring DFT metal slab artefacts, affected trajectories are marked with "*" (c.f. Sec. VIIIa).

| system | $\langle \Delta E_{\mathrm{ad}}^{\mathrm{total}} \rangle$ (eV) | | | | $\frac{dE^{\mathrm{total}}}{dt}$ (meV/ps) | | | |
|---|---|---|---|---|---|---|---|---|
| | #1 | #2 | #3 | #4 | #1 | #2 | #3 | #4 |
| Cu(211) | -0.06 | 0.02 | 0.01 | 0.03 | -7 | 6 | 9 | -4 |
| CO/Cu(211) | -0.80 | -0.69 | -0.83 | -0.59 | 1 | -8 | -1 | 13 |
| CHO/Cu(211) | -0.51 | -0.35 | -0.71 | -0.54 | 1 | 7 | -12 | -29 |
| COH/Cu(211) | -0.16 | 0.08 | -0.44 | -0.47 | -31 | -14 | -24 | -20 |
| OCCHO/Cu(211) | -0.87 | -1.20 | -0.97 | -1.13 | -23 | 6 | -8 | -10 |
| OH/Cu(211) | -0.28 | -0.35 | -0.25 | -0.28 | -5 | -8 | -7 | 2 |
| Cu(111) | 0.07 | -0.12 | 0.01 | 0.03 | -1 | -12 | 17 | 11 |
| CO/Cu(111) | -0.87 | -0.74 | -0.69 | -0.91 | 1 | 16 | -20 | -7 |
| OH/Cu(111) | -0.22 | -0.13 | -0.26 | -0.12 | -7 | -14 | -3 | -12 |
| Au(111) | 0.15 | 0.08 | -0.22 | -0.01 | -2 | -21 | -28 | -2 |
| CO/Au(111) | -0.29 | -0.34 | -0.23 | -0.19 | -21 | -45 | -22 | -4 |
| OH/Au(111) | 0.60 | 0.38 | 0.53 | 0.59 | -2 | 0 | -12 | -19 |
| OOH/Au(111) | 3.91 | 4.12 | 3.85 | 3.91 | -16 | -14 | -9 | -61 |
| Pt(111) | -0.04 | -0.07 | 0.11 | 0.03 | 13 | -22 | -29 | -11 |
| CO/Pt(111) | -1.85 | -2.14 | -1.99 | -2.47 | 11 | 5 | -21 | 1 |
| OH/Pt(111) | 0.13 | 0.14 | 0.09 | -0.00 | -10 | 3 | -7 | 2 |
| OOH/Pt(111) | 2.92 | 3.46 | 3.56* | 3.48* | -10 | -29 | -25* | 77* |

# II Metal-water radial distribution functions

We monitor the metal-water interface via a radial distribution function (RDF) between the top-layer metal atoms (Me) and the hydrogen (H) and oxygen atoms (O) of the water molecules. This delivers a complementary picture to the density profiles presented in Sec. III A in the main text.

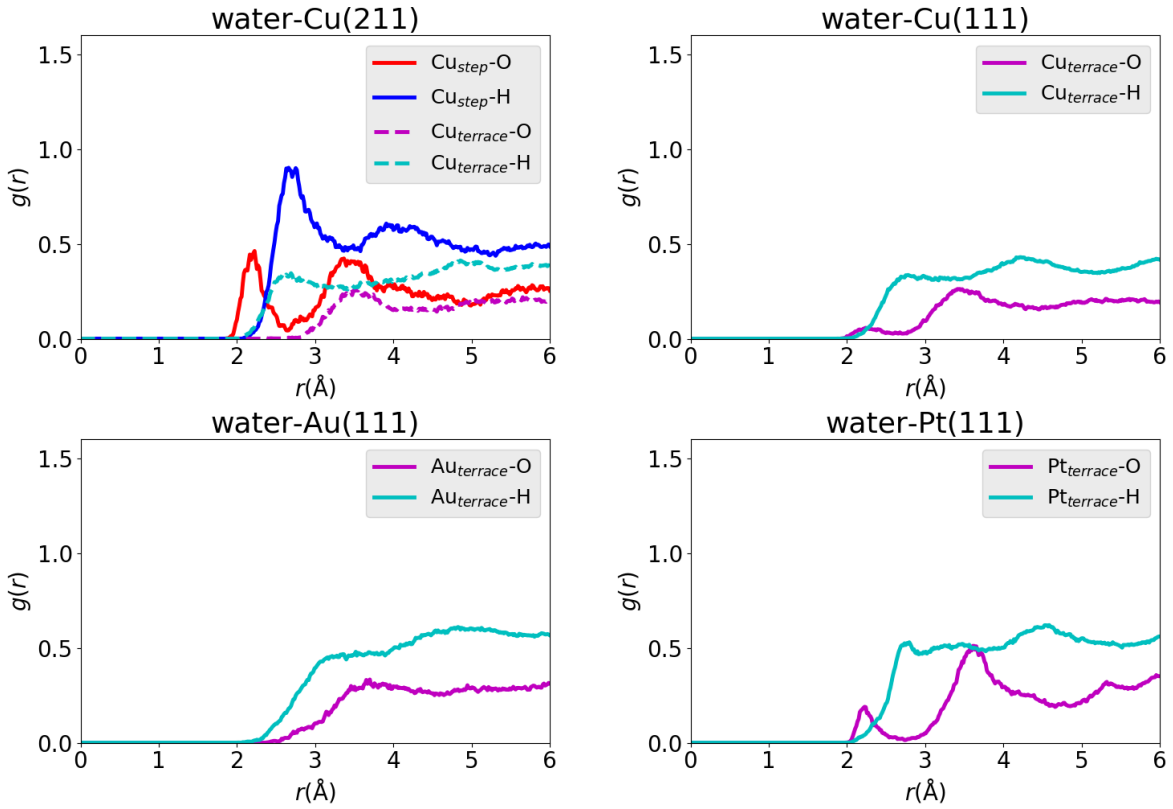


Figure S2: Radial distribution function $g(r)$ of the Me-$O_{H_2O}$ distance with Me = Cu(211) (top left), Cu(111) (top right), Au(111) (bottom left), and Pt(111) (bottom right).

As shown in Fig. S2, the Me-O RDFs of the Cu(211), Cu(111), and Pt(111) surfaces show a water-bilayer structure visible through a double peak at $r$=2-4 Å. While this is also reflected in the density profiles of Cu(111) and Pt(111) (see main text), it is not obvious in the density profile of Cu(211). For the latter, it can be seen that the bilayer structure forms primarily around the step edge. We use the RDFs to determine a criterion for water adsorption. In that, 2.55 Å is chosen, which is the distance including the first bilayer peak for the Cu and Pt surface and the onset of the water boundary on Au(111).

# III Adsorption and solvation energies

The adsorption and solvation energies obtained through geometry optimizations in presence (and absence) of implicit solvent for all adsorbate/surface combinations are depicted in Tab. S2, S3, and S4. Included are all sites which were sampled during the respective AIMD simulations. The labeling of the symmetrically inequivalent sites of same coordination symmetry follows alphabetical order. That means, that among all top, bridge, threefold hollow (hollow3) or fourfold hollow (hollow4) sites a tag "-a", "-b", ... is introduced (c.f. Fig. S3).

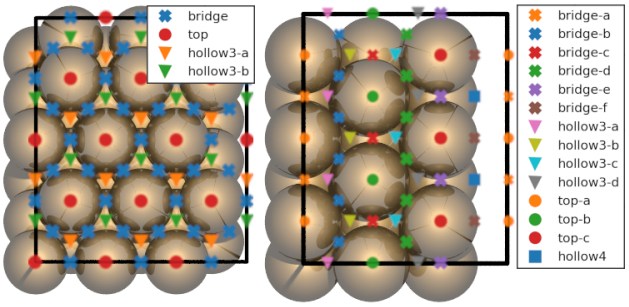


Figure S3: Surface sites for the 3×4-(111) (left) and 3×1-(211) (right) slab models used for the site-partitioning of the AIMD trajectories. Symmetrically equivalent sites are shown in the same color.

It can be seen in Tab. S2, S3, and S4 that in most cases the relative share of occupation during an AIMD trajectory $r_{\text{site}}$ matches the relative stability of the respective adsorption sites obtained from the geometry optimizations. The only outliers to this trend are *CHO on Cu(211) and *OH on Au(111). In the former, $> 50\,\%$ of occupied, less favorable sites ($\Delta\Delta E_{\text{ad}} \approx 0.1\,\text{eV}$) belong to the (111) terrace moiety of the (211) step. It is likely that the high mobility of *CHO (c.f. Fig. 2 in the main text) leads to the partial occupation of these (more abundant) sites. In the case of *OH on Au(111), the preference for the less stable top site ($\Delta\Delta E_{\text{ad}} \approx 0.15\,\text{eV}$) is likely due to a considerably increased adsorbate-water interaction and therefore higher solvation stabilization in comparison to the bridge or hollow sites.

In order to generalize the findings for the electron density dependent (GLSSA13)[1] implicit solvent model as implemented in VASPsol,[2] we evaluate all adsorption and solvation energies

Table S2: Adsorption and solvation energies ($\Delta E_{\mathrm{ad}}$ and $\Delta E_{\mathrm{sol}}$) in eV computed via geometry optimizations at all adsorption sites probed during the AIMD simulations. Additional to the VASPsol results (see main text) the optimized energies in Quantum ESPRESSO / Environ (QE-SCCS) are depicted. The overall site-occupation ratio $r_{\mathrm{site}}$ and the residence time $\tau$ during the AIMD simulations for each site are shown as well. See Fig. S3 for an explanation of the site labels.

| | $\Delta E_{\mathrm{ad}}^{\mathrm{VASPsol}}$ | $\Delta E_{\mathrm{sol}}^{\mathrm{VASPsol}}$ | $\Delta E_{\mathrm{ad}}^{\mathrm{QE\text{-}SCCS}}$ | $\Delta E_{\mathrm{sol}}^{\mathrm{QE\text{-}SCCS}}$ | $r_{\mathrm{site}}$ | $\tau$ (fs) |
|---|---|---|---|---|---|---|
| | CO / Cu(211) | | | | | |
| top-c | -0.97 | 0.00 | -0.93 | 0.00 | 0.12 | 596 |
| bridge-f | -0.95 | 0.00 | -0.89 | 0.00 | 0.01 | 228 |
| hollow3-c | -0.94 | -0.01 | -0.88 | 0.00 | 0.03 | 481 |
| bridge-d | -0.94 | -0.01 | -0.88 | 0.00 | 0.10 | 238 |
| hollow3-d | -0.94 | 0.00 | -0.87 | 0.00 | 0.29 | 393 |
| bridge-e | -0.94 | 0.00 | -0.93 | 0.00 | 0.43 | 761 |
| bridge-c | -0.93 | -0.01 | -0.88 | 0.00 | 0.01 | $\leq 50$ |
| | CHO / Cu(211) | | | | | |
| hollow4 | -0.66 | -0.09 | -0.53 | -0.09 | 0.02 | 316 |
| bridge-b | -0.62 | -0.11 | -0.53 | -0.09 | 0.10 | 266 |
| bridge-d | -0.61 | -0.08 | -0.52 | -0.08 | 0.00 | 218 |
| top-c | -0.61 | -0.12 | -0.52 | -0.10 | 0.16 | 474 |
| bridge-f | -0.56 | -0.10 | -0.49 | -0.09 | 0.03 | 380 |
| top-b | -0.51 | -0.08 | -0.35 | -0.08 | 0.34 | 481 |
| bridge-e | -0.51 | -0.08 | -0.30 | -0.06 | 0.28 | 668 |
| bridge-c | -0.51 | -0.08 | -0.30 | -0.06 | 0.03 | 158 |
| hollow3-b | -0.48 | -0.09 | -0.39 | -0.09 | 0.03 | 342 |
| hollow3-d | -0.41 | -0.03 | -0.34 | -0.04 | 0.00 | 0 |
| hollow3-c | -0.37 | -0.04 | -0.29 | -0.04 | 0.00 | 0 |

based on Quantum ESPRESSO / Environ.[3,4] For this, we employ geometry optimizations in presence and absence of the self-consistent continuum solvation (SCCS) implicit solvent model on the same adjusted slab models. The computational details are kept equivalent where possible, with the same RPBE-D3 functional[5–7] and using the same Monkhorst-Pack k-point grids. Otherwise, plane-wave and density cutoffs of 500 and 5000 eV and a Fermi-smearing width of 0.1 eV were used. The electronic structure was converged until a total energy difference of $10^{-5}$ eV. For the employed slab models, the lattice constants are adjusted based on the computational details and converged to 3.694 Å for Cu, 4.229 Å for Au, and

4.018 Å for Pt.

Table S3: Adsorption and solvation energies ($\Delta E_{\mathrm{ad}}$ and $\Delta E_{\mathrm{sol}}$) in eV computed via geometry optimizations at all adsorption sites probed during the AIMD simulations. Additional to the VASPsol results (see main text) the optimized energies in Quantum ESPRESSO / Environ (QE-SCCS) are depicted. The overall site-occupation ratio $r_{\mathrm{site}}$ and the residence time $\tau$ during the AIMD simulations for each site are shown as well. See Fig. S3 for an explanation of the site labels.

| | $\Delta E_{\mathrm{ad}}^{\mathrm{VASPsol}}$ | $\Delta E_{\mathrm{sol}}^{\mathrm{VASPsol}}$ | $\Delta E_{\mathrm{ad}}^{\mathrm{QE\text{-}SCCS}}$ | $\Delta E_{\mathrm{sol}}^{\mathrm{QE\text{-}SCCS}}$ | $r_{\mathrm{site}}$ | $\tau$ (fs) |
|---|---|---|---|---|---|---|
| | COH / Cu(211) | | | | | |
| bridge-a | 0.00 | -0.02 | 0.12 | -0.09 | 0.13 | 220 |
| hollow4 | 0.00 | -0.13 | 0.14 | -0.18 | 0.87 | 515 |
| | OCCHO / Cu(211) | | | | | |
| bridge-d | -1.31 | -0.16 | -1.17 | -0.12 | 0.06 | 439 |
| hollow3-c | -1.30 | -0.17 | -1.13 | -0.10 | 0.02 | 866 |
| top-c | -1.29 | -0.15 | -1.17 | -0.14 | 0.23 | 643 |
| bridge-e | -1.27 | -0.15 | -1.20 | -0.13 | 0.65 | 3488 |
| bridge-f | -1.22 | -0.19 | -1.00 | -0.01 | 0.01 | 324 |
| hollow3-d | -1.18 | -0.05 | -1.05 | -0.10 | 0.02 | 253 |
| bridge-b | -1.16 | -0.17 | -1.02 | -0.13 | 0.03 | 0 |
| | OH / Cu(211) | | | | | |
| hollow3-d | -0.53 | -0.12 | -0.27 | -0.07 | 0.01 | 192 |
| bridge-e | -0.52 | -0.10 | -0.51 | -0.10 | 0.97 | 4434 |
| top-c | -0.52 | -0.09 | -0.50 | -0.11 | 0.01 | 336 |
| hollow4 | -0.52 | -0.09 | -0.50 | -0.10 | 0.01 | 177 |

The adsorption energies obtained from the two employed DFT codes are in most cases very similar and only differ in some cases with a maximum deviation of $\leq 0.2$ eV. We attribute these deviations to the difference in the PAW-formalism in VASP and the employed ultra-soft pseudopotentials. In contrast to this, the contribution of the implicit solvent model and thus the solvation energies are near-identical. This indicates, that the here presented shortcomings for continuum solvation methods are of general nature. It should be noted, that we omitted more rigorous solvation schemes like RISM or CANDLE (see main text). These may account for some of the directional contributions and thus improve the continuum solvation energies.

Table S4: Adsorption and solvation energies ($\Delta E_{\mathrm{ad}}$ and $\Delta E_{\mathrm{sol}}$) in eV computed via geometry optimizations at all adsorption sites probed during the AIMD simulations. Additional to the VASPsol results (see main text) the optimized energies in Quantum ESPRESSO / Environ (QE-SCCS) are depicted. The overall site-occupation ratio $r_{\mathrm{site}}$ and the residence time $\tau$ during the AIMD simulations for each site are shown as well. See Fig. S3 for an explanation of the site labels.

| | $\Delta E_{\mathrm{ad}}^{\mathrm{VASPsol}}$ | $\Delta E_{\mathrm{sol}}^{\mathrm{VASPsol}}$ | $\Delta E_{\mathrm{ad}}^{\mathrm{QE\text{-}SCCS}}$ | $\Delta E_{\mathrm{sol}}^{\mathrm{QE\text{-}SCCS}}$ | $r_{\mathrm{site}}$ | $\tau$ (fs) |
|---|---|---|---|---|---|---|
| | CO / Cu(111) | | | | | |
| hollow3-b | -0.88 | -0.02 | -0.78 | -0.00 | 0.22 | 434 |
| hollow3-a | -0.87 | -0.02 | -0.78 | -0.00 | 0.28 | 423 |
| top | -0.85 | -0.01 | -0.81 | 0.01 | 0.04 | 411 |
| bridge | -0.85 | -0.01 | -0.81 | 0.01 | 0.46 | 301 |
| | OH / Cu(111) | | | | | |
| bridge | 0.03 | -0.08 | -0.03 | -0.09 | 0.58 | 501 |
| hollow3-a | 0.07 | -0.08 | -0.07 | -0.08 | 0.13 | 423 |
| hollow3-b | 0.07 | -0.08 | -0.06 | -0.08 | 0.12 | 343 |
| top | 0.17 | -0.09 | 0.38 | -0.16 | 0.17 | 458 |
| | CO / Au(111) | | | | | |
| top | -0.39 | -0.00 | -0.39 | -0.00 | 0.33 | 747 |
| hollow3-b | -0.37 | 0.01 | -0.37 | 0.01 | 0.13 | 340 |
| bridge | -0.37 | 0.01 | -0.36 | 0.01 | 0.47 | 429 |
| hollow3-a | -0.20 | -0.03 | -0.36 | 0.01 | 0.07 | 290 |
| | OH / Au(111) | | | | | |
| bridge | 1.00 | -0.07 | 0.98 | -0.08 | 0.30 | 344 |
| hollow3-b | 1.00 | -0.07 | 0.97 | -0.08 | 0.03 | 299 |
| hollow3-a | 1.04 | -0.07 | 1.08 | -0.02 | 0.14 | 434 |
| top | 1.14 | -0.18 | 1.15 | -0.15 | 0.54 | 788 |
| | OOH / Au(111) | | | | | |
| top | 4.10 | -0.12 | 4.15 | -0.18 | 0.62 | 699 |
| bridge | 4.11 | -0.18 | 4.07 | -0.15 | 0.28 | 298 |
| hollow3-a | 4.16 | -0.19 | 4.10 | -0.16 | 0.06 | 286 |
| hollow3-b | 4.16 | -0.20 | 4.10 | -0.16 | 0.04 | 373 |
| | CO / Pt(111) | | | | | |
| bridge | -1.89 | -0.00 | -1.85 | -0.03 | 0.64 | 441 |
| hollow3-a | -1.89 | -0.00 | -1.84 | -0.03 | 0.25 | 514 |
| hollow3-b | -1.88 | -0.01 | -1.84 | -0.03 | 0.11 | 838 |
| | OH / Pt(111) | | | | | |
| top | 0.62 | -0.12 | 0.62 | -0.14 | 0.99 | 1801 |
| bridge | 0.71 | -0.13 | 0.65 | -0.13 | 0.01 | 0 |
| | OOH / Pt(111) | | | | | |
| top | 3.43 | -0.18 | 3.62 | -0.22 | 0.96 | 2397 |
| bridge | 3.77 | -0.20 | 3.73 | -0.21 | 0.04 | 231 |

Table S5: Average adsorption and solvation energies ($\Delta E_{\mathrm{ad}}$ and $\Delta E_{\mathrm{sol}}$) of all adsorbate/surface combinations in eV as obtained from the AIMD simulations (see main text). These values correspond to the data points in Fig. 8 in the main text.

| | $\Delta E_{\mathrm{ad}}$ | $\Delta E_{\mathrm{sol}}$ |
|---|---|---|
| | Cu(211) | |
| CO | -0.69 ± 0.05 | 0.24 ± 0.05 |
| CHO | -0.35 ± 0.05 | 0.09 ± 0.05 |
| COH | 0.31 ± 0.05 | 0.12 ± 0.05 |
| OCCHO | -0.99 ± 0.08 | -0.09 ± 0.08 |
| OH | -0.29 ± 0.03 | -0.004 ± 0.03 |
| | Cu(111) | |
| CO | -0.77 ± 0.06 | 0.01 ± 0.06 |
| OH | -0.11 ± 0.05 | -0.32 ± 0.05 |
| | Au(111) | |
| CO | -0.26 ± 0.07 | -0.14 ± 0.07 |
| OH | 0.53 ± 0.08 | -0.68 ± 0.08 |
| OOH | 3.93 ± 0.09 | -0.48 ± 0.09 |
| | Pt(111) | |
| CO | -2.07 ± 0.12 | -0.15 ± 0.12 |
| OH | 0.11 ± 0.07 | -0.58 ± 0.07 |
| OOH | 3.55 ± 0.06 | -0.05 ± 0.06 |

The average adsorption and solvation energies obtained from the AIMD simulations as described in the main text are given in Tab. S5. This data corresponds to Fig. 8 in the main text. Note that the uncertainties of respective adsorption and solvation energies are identical. Both properties are related through the adsorption energy without solvent (Eq. 3 in the main text) for which we do not determine an error (as we found it negligible).

# IV Detailed tables for competitive water adsorption

Table S6: $H_2O$ adsorption statistics for Cu(211) with and without (clean) the presence of adsorbates including the site-resolution. Displayed are the average number of $H_2O$ molecules adsorbed ($\langle n_{\mathrm{ad}}^{\mathrm{H_2O}} \rangle$), the frequency of $H_2O$ adsorption ($f_{\mathrm{ad}}^{\mathrm{H_2O}}$) and the average residence time of $H_2O$ molecules ($\langle \tau \rangle$) on the surface. Sites with less than 1 % $H_2O$ adsorbed are not shown. See Fig. S3 for an explanation of the site labels.

| site | $\langle n_{\mathrm{ad}}^{\mathrm{H_2O}} \rangle$ | $f_{\mathrm{ad}}$ ($\mathrm{ps}^{-1}$) | $\langle \tau \rangle$ (fs) |
|---|---|---|---|
| clean Cu(211) | | | |
| total | 1.68 | 2.95 | 599 |
| top-c | 1.53 | 1.25 | 1262 |
| bridge-e | 0.08 | 0.70 | 124 |
| bridge-f | 0.05 | 0.59 | 128 |
| bridge-d | 0.01 | 0.18 | 48 |
| hollow4 | 0.01 | 0.10 | 82 |
| CO / Cu(211) | | | |
| total | 1.23 | 2.35 | 540 |
| top-c | 1.08 | 0.69 | 1602 |
| bridge-e | 0.08 | 0.73 | 121 |
| top-b | 0.03 | 0.13 | 224 |
| bridge-f | 0.02 | 0.43 | 61 |
| bridge-d | 0.01 | 0.23 | 60 |
| CHO / Cu(211) | | | |
| total | 1.22 | 2.18 | 596 |
| top-c | 0.91 | 0.77 | 1260 |
| bridge-e | 0.20 | 0.60 | 355 |
| top-b | 0.08 | 0.32 | 262 |
| bridge-f | 0.01 | 0.16 | 98 |
| bridge-b | 0.01 | 0.14 | 37 |

Table S7: $H_2O$ adsorption statistics for Cu(211) with and without (clean) the presence of adsorbates including the site-resolution. Displayed are the average number of $H_2O$ molecules adsorbed ($\langle n_{\mathrm{ad}}^{\mathrm{H_2O}} \rangle$), the frequency of $H_2O$ adsorption ($f_{\mathrm{ad}}^{\mathrm{H_2O}}$) and the average residence time of $H_2O$ molecules ($\langle \tau \rangle$) on the surface. Sites with less than 1 % $H_2O$ adsorbed are not shown. See Fig. S3 for an explanation of the site labels.

| site | $\langle n_{\mathrm{ad}}^{\mathrm{H_2O}} \rangle$ | $f_{\mathrm{ad}}$ ($\mathrm{ps}^{-1}$) | $\langle \tau \rangle$ (fs) |
|---|---|---|---|
| COH / Cu(211) | | | |
| total | 0.34 | 0.51 | 697 |
| top-c | 0.30 | 0.19 | 1603 |
| bridge-e | 0.01 | 0.12 | 131 |
| top-b | 0.01 | 0.06 | 240 |
| bridge-f | 0.01 | 0.07 | 146 |
| OCCHO / Cu(211) | | | |
| total | 2.15 | 3.11 | 718 |
| top-b | 1.04 | 0.58 | 1901 |
| top-c | 0.93 | 0.23 | 4096 |
| bridge-e | 0.08 | 0.40 | 203 |
| bridge-b | 0.04 | 0.89 | 58 |
| bridge-c | 0.02 | 0.39 | 66 |
| bridge-f | 0.01 | 0.15 | 133 |
| bridge-d | 0.01 | 0.20 | 68 |
| OH / Cu(211) | | | |
| total | 1.23 | 2.15 | 589 |
| top-c | 0.89 | 0.17 | 5182 |
| top-b | 0.27 | 0.70 | 418 |
| bridge-e | 0.03 | 0.50 | 72 |
| bridge-f | 0.01 | 0.12 | 106 |
| bridge-b | 0.01 | 0.29 | 38 |
| bridge-d | 0.01 | 0.16 | 65 |

Table S8: $H_2O$ adsorption statistics for Cu(111) with and without (clean) the presence of adsorbates including the site-resolution. Displayed are the average number of $H_2O$ molecules adsorbed ($\langle n_{\mathrm{ad}}^{\mathrm{H_2O}} \rangle$), the frequency of $H_2O$ adsorption ($f_{\mathrm{ad}}^{\mathrm{H_2O}}$) and the average residence time of $H_2O$ molecules ($\langle \tau \rangle$) on the surface. Sites with less than 1 % $H_2O$ adsorbed are not shown. See Fig. S3 for an explanation of the site labels.

| site | $\langle n_{\mathrm{ad}}^{\mathrm{H_2O}} \rangle$ | $f_{\mathrm{ad}}$ ($\mathrm{ps}^{-1}$) | $\langle \tau \rangle$ (fs) |
|---|---|---|---|
| clean Cu(111) | | | |
| total | 1.42 | 6.35 | 240 |
| top | 1.13 | 2.08 | 578 |
| bridge | 0.23 | 3.21 | 80 |
| hollow3-b | 0.04 | 0.65 | 60 |
| hollow3-a | 0.02 | 0.41 | 67 |
| CO / Cu(111) | | | |
| total | 1.18 | 4.82 | 264 |
| top | 0.99 | 1.78 | 598 |
| bridge | 0.16 | 2.40 | 71 |
| hollow3-b | 0.02 | 0.38 | 62 |
| hollow3-a | 0.01 | 0.26 | 52 |
| OH / Cu(111) | | | |
| total | 1.11 | 3.99 | 301 |
| top | 0.97 | 1.87 | 564 |
| bridge | 0.11 | 1.70 | 73 |
| hollow3-b | 0.01 | 0.21 | 62 |
| hollow3-a | 0.01 | 0.21 | 54 |

Table S9: $H_2O$ adsorption statistics for Au(111) with and without (clean) the presence of adsorbates including the site-resolution. Displayed are the average number of $H_2O$ molecules adsorbed ($\langle n_{\mathrm{ad}}^{\mathrm{H_2O}} \rangle$), the frequency of $H_2O$ adsorption ($f_{\mathrm{ad}}^{\mathrm{H_2O}}$) and the average residence time of $H_2O$ molecules ($\langle \tau \rangle$) on the surface. Sites with less than 1 % $H_2O$ adsorbed are not shown. See Fig. S3 for an explanation of the site labels.

| site | $\langle n_{\mathrm{ad}}^{\mathrm{H_2O}} \rangle$ | $f_{\mathrm{ad}}$ ($\mathrm{ps}^{-1}$) | $\langle \tau \rangle$ (fs) |
|---|---|---|---|
| clean Au(111) | | | |
| total | 0.07 | 1.30 | 58 |
| top | 0.05 | 0.93 | 61 |
| bridge | 0.01 | 0.22 | 48 |
| hollow3-b | 0.01 | 0.11 | 64 |
| CO / Au(111) | | | |
| total | 0.03 | 0.56 | 48 |
| top | 0.02 | 0.38 | 53 |
| bridge | 0.01 | 0.13 | 44 |
| OH / Au(111) | | | |
| total | 1.04 | 9.98 | 123 |
| top | 0.60 | 4.73 | 150 |
| bridge | 0.30 | 3.62 | 97 |
| hollow3-a | 0.09 | 1.12 | 102 |
| hollow3-b | 0.04 | 0.51 | 97 |
| OOH / Au(111) | | | |
| total | 0.49 | 5.58 | 102 |
| top | 0.30 | 2.78 | 131 |
| bridge | 0.12 | 1.83 | 73 |
| hollow3-a | 0.04 | 0.59 | 74 |
| hollow3-b | 0.03 | 0.38 | 77 |

Table S10: $H_2O$ adsorption statistics for Pt(111) with and without (clean) the presence of adsorbates including the site-resolution. Displayed are the average number of $H_2O$ molecules adsorbed ($\langle n_{\mathrm{ad}}^{\mathrm{H_2O}} \rangle$), the frequency of $H_2O$ adsorption ($f_{\mathrm{ad}}^{\mathrm{H_2O}}$) and the average residence time of $H_2O$ molecules ($\langle \tau \rangle$) on the surface. Sites with less than 1 % $H_2O$ adsorbed are not shown. See Fig. S3 for an explanation of the site labels.

| site | $\langle n_{\mathrm{ad}}^{\mathrm{H_2O}} \rangle$ | $f_{\mathrm{ad}}$ ($\mathrm{ps}^{-1}$) | $\langle \tau \rangle$ (fs) |
|---|---|---|---|
| clean Pt(111) | | | |
| total | 1.83 | 1.44 | 1328 |
| top | 1.81 | 0.98 | 1931 |
| bridge | 0.02 | 0.40 | 53 |
| CO / Pt(111) | | | |
| total | 1.92 | 2.48 | 807 |
| top | 1.87 | 1.23 | 1577 |
| bridge | 0.04 | 1.07 | 44 |
| OH / Pt(111) | | | |
| total | 1.05 | 1.19 | 946 |
| top | 1.04 | 1.01 | 1101 |
| bridge | 0.01 | 0.16 | 54 |
| OOH / Pt(111) | | | |
| total | 0.99 | 0.97 | 1073 |
| top | 0.97 | 0.69 | 1471 |
| bridge | 0.02 | 0.24 | 75 |

# V Solvation energy relationships

## Va Correlations to deviation of continuum solvation energies

The correlation against hydrogen bonding $n_{\mathrm{Hbond}}$ and competitive water adsorption $\Delta\langle n_{\mathrm{ad}}^{\mathrm{H_2O}}\rangle$ of the solvation energy (see main text), equally fits to the difference of solvation energies $\Delta\Delta E_{\mathrm{solv}}^{\text{aimd-impl}}$ between AIMD and continuum solvation. As depicted in Fig. S4, the $\Delta\Delta E_{\mathrm{solv}}^{\text{aimd-impl}}$ gives a clear cut correlation with both quantities. The corresponding linear relationships of the small adsorbates follow for hydrogen bonding as $f = 1.57\,\mathrm{eV} - (0.74 \cdot \langle n_{\mathrm{Hbond}}\rangle)\,\mathrm{eV}$ and for competitive water adsorption as $f = -0.15\,\mathrm{eV} - (0.79 \cdot \Delta\langle n_{\mathrm{ad}}^{\mathrm{H_2O}}\rangle)\,\mathrm{eV}$.

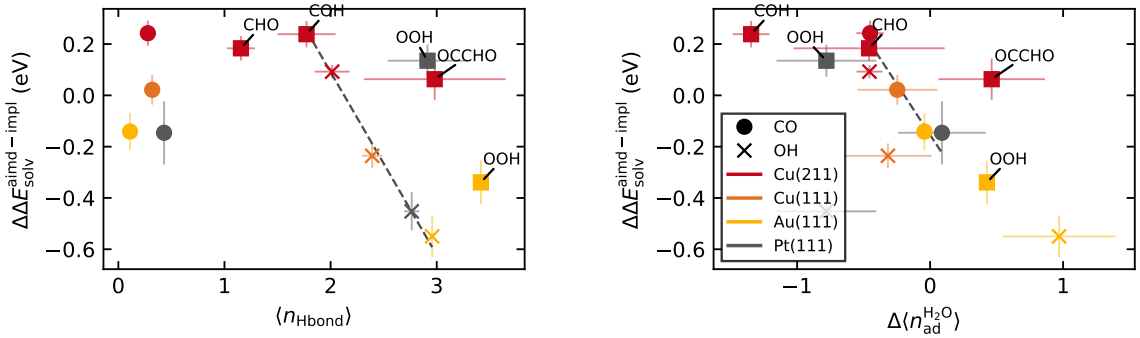


Figure S4: Difference of the solvation energy between AIMD and continuum solvation $\Delta\Delta E_{\mathrm{solv}}^{\text{aimd-impl}}$ against the average number of Hbonds $\langle n_{\mathrm{Hbond}}\rangle$ (left) and against the difference in average number of adsorbed water molecules in presence of an adsorbate against the clean surface $\Delta\langle n_{\mathrm{ad}}^{\mathrm{H_2O}}\rangle$ (right). Apparent correlations (see text) are indicated by the dark dashed lines.

## Vb Towards the prediction of hydrogen bonding and water adsorption at the metal/water interface

The quantified linear correlation of solvation energies with the hydrogen bonding $\langle n_{\mathrm{Hbond}}\rangle$ and competitive water adsorption $\Delta\langle n_{\mathrm{ad}}^{\mathrm{H_2O}}\rangle$ suggest a underlying physical relationship. This relationship may in turn be exploited to predict accurate solvation energies without the need for costly AIMD simulations. In order to do so, $\langle n_{\mathrm{Hbond}}\rangle$ and $\langle n_{\mathrm{ad}}^{\mathrm{H_2O}}\rangle$ need to be predictable from reliably determinable descriptors. We correlate $\langle n_{\mathrm{Hbond}}\rangle$ and $\Delta\langle n_{\mathrm{ad}}^{\mathrm{H_2O}}\rangle$ (or

$\langle n_{\mathrm{ad}}^{\mathrm{H_2O}} \rangle$) against a number of descriptors including surface dipole moments, Bader charges, workfunction and solvation/adsorption energies from microsolvation models. For clarity we only present the descriptors showing highest correlations.

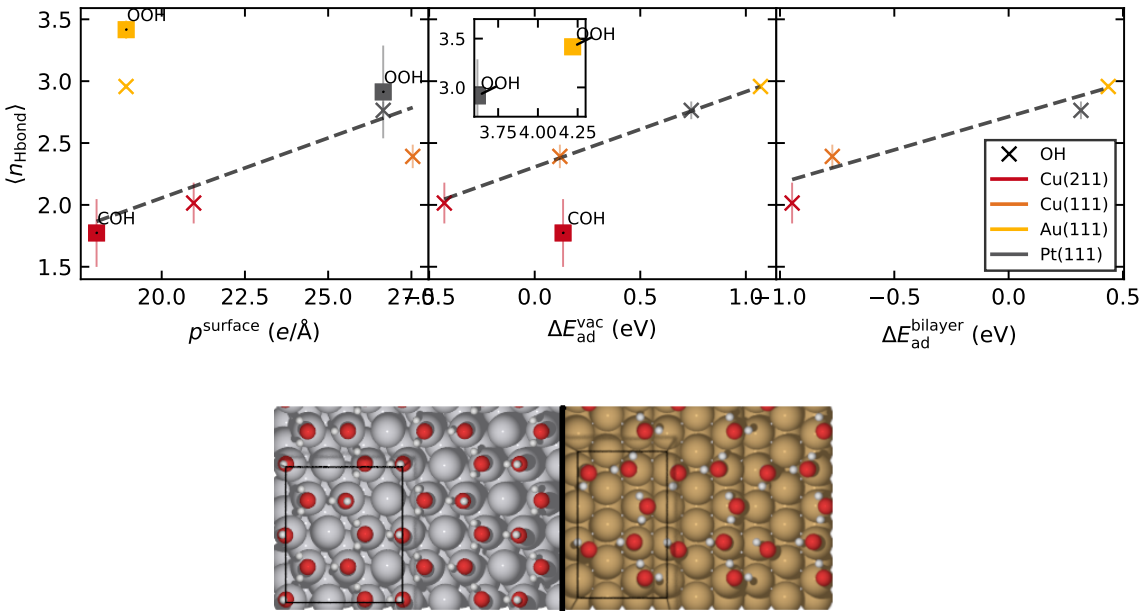


Figure S5: (top) Correlation of hydrogen bonding with the surface dipole moment $p^{\mathrm{surface}}$ (left), adsorption energy at the metal/vacuum interface $\Delta E_{\mathrm{ad}}^{\mathrm{vac}}$ (center) and adsorption energy of *OH in presence of a complete ice-like bilayer $\Delta E_{\mathrm{ad}}^{\mathrm{bilayer}}$ (right). Apparent correlations (see text) are indicated by the dark dashed lines. (bottom) Examples of the water bilayer structure incorporating *OH on Pt(111) (left) and Cu(211) (right).

For the hydrogen bonding we find some correlation with the surface dipole moment of the adsorbate at the metal/vacuum interface and adsorption energies determined in vacuum and in presence of a static water bilayer. As shown in Fig. S5, the surface dipole moment correlates $\langle n_{\mathrm{Hbond}} \rangle$ across the adsorbates *OH, *OOH and *COH and metal facets Cu(211), Cu(111), Pt(111) with a moderate error of $\approx 0.1$. Two significant outliers with a deviation according to $\approx$ 0.8-1.3 are *OH and *OOH on Au(111). The physical explanation for Au(111) containing all outliers is likely due to the fundamental change in the metal/water interface due to the coadsorption of adsorbate and water. Originating in the "anchoring effect" of the *OH group, which is not as dramatic for the other surfaces, the water is significantly closer to the Au(111) surface, changing the apparent surface dipole in the AIMD simulation

(see Sec. III A in the main text). This deviation disqualifies the surface dipole moment as a reliable descriptor. More consistently, the adsorption energies among the *OH adsorbates at the metal/vacuum interface scale with $\langle n_{\mathrm{Hbond}} \rangle$. This trend does, however, exclude *COH on Cu(211), and *OOH on Au(111) and Pt(111) and may thus only be relevant among same types of adsorbates – similar to the general scaling relations for adsorption energies.[8] We can formulate a model to predict solvation energies specifically for *OH on metal surfaces from this correlation in combination with our solvation energy-$\langle n_{\mathrm{Hbond}} \rangle$ relationship (see main text). A function for the solvation energy of *OH ($\Delta E_{\mathrm{solv}}^{^*\mathrm{OH}}$) follows as $\Delta E_{\mathrm{solv}}^{^*\mathrm{OH}} = -0.22\,\mathrm{eV} - 0.44 \cdot \Delta E_{\mathrm{ad}}^{\mathrm{vac},^*\mathrm{OH}}$. This function yields an increasing solvation energy with a weaker binding strength of the *OH to the metal surface. The *OOH adsorbates, on baseis of two data points, also tentatively appear to follow a similar trend but with a different gradient and intercept ($\Delta E_{\mathrm{solv}}^{^*\mathrm{OOH}} = 2.55\,\mathrm{eV} - 0.72 \cdot \Delta E_{\mathrm{ad}}^{\mathrm{vac},^*\mathrm{OOH}}$). Finally, a correlation of $\langle n_{\mathrm{Hbond}} \rangle$ to *OH adsorption energies in the presence of a static bilayer also retain the previous trend. However, the setup of a static bilayer is in no way straight forward. While a hexagonal bilayer is commonly used on a Pt(111) surface[9] its realization is not clear on other metals or facets as shown for the example of Cu(211) in Fig. S5. A sampling problem follows this issue. As a consequence, the data suffers from considerable scatter and an unsystematic "correction" follows for the adsorption energies. The latter, leads to a slight improvement for Pt(111) and Au(111) but a clear worsening for Cu(111) and Cu(211) in comparison to the AIMD values (see main text). Further, we could not stabilize *COH in presence of a static water bilayer. Such practical issues disqualify static water layer models for the reliable prediction of specific properties of metal/water interfaces.

In the case of the average water adsorption $\langle n_{\mathrm{ad}}^{\mathrm{H_2O}} \rangle$ at the pure metal/water interface, we find very good correlation of its top-site normalized value with the (most stable) adsorption energy of a single water molecule at the metal/vacuum interface as shown in Fig. S6. While this result is quite intuitive, it confirms hydrophilicity as an atomistic/microscopic property. Consolidating the competitive water adsorption $\Delta \langle n_{\mathrm{ad}}^{\mathrm{H_2O}} \rangle$ is, however, at this point unclear.

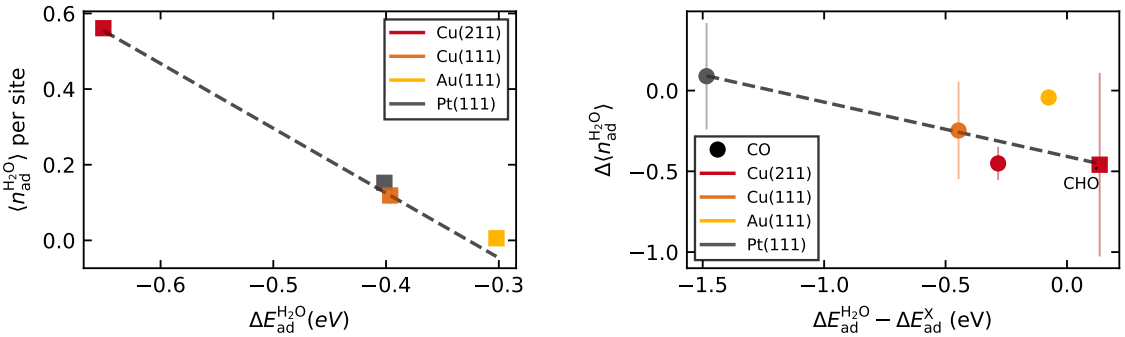


Figure S6: (left) Correlation for the amount of the top-site normalized water adsorption $\langle n_{\mathrm{ad}}^{\mathrm{H_2O}} \rangle$ with the lowest adsorption energy of a single water molecule at the metal/vacuum interface ($\Delta E_{\mathrm{ad}}^{\mathrm{H_2O}}$). (right) Correlation of the difference of water adsorption upon presence of an adsorbate ($\Delta\langle n_{\mathrm{ad}}^{\mathrm{H_2O}} \rangle$) against the difference in adsorption energy of a single water molecule and the respective adsorbate $x$ ($\Delta E_{\mathrm{ad}}^{\mathrm{H_2O}} - \Delta E_{\mathrm{ad}}^{\mathrm{x}}$).

We only can show a weak correlation between the difference in binding energy of an adsorbate and a water molecule (c.f. Fig. S6). Excluded from this correlation is CO on Au(111). It should be noted, that the latter outlier does not show any water adsorption ($\langle n_{\mathrm{ad}}^{\mathrm{H_2O}} \rangle$=0). In such a case, competitive water adsorption does not play a role. To capture this exception a $\langle n_{\mathrm{ad}}^{\mathrm{H_2O}} \rangle$=0 criterion would be needed as an additional descriptor for the prediction of competitive water adsorption.

# VI Estimation of the hydration entropy of adsorbates on metal surfaces

Implicit solvation models are usually parameterized to experimentally determined free energies of solvation. The free energy component in the implicit solvation thereby contains the hydration entropy change upon cavitation of a solute. This property scales with the size of a solute, specifically with its solvent accessible surface area (SASA).[10] This linear relationship is shown in Fig. S7 for alkanes in water (at 300K). We employ this relationship to estimate the hydration entropies for all adsorbate-surface combinations in our test set. We deem this approach feasible since organic molecules including polar functional groups like amides,

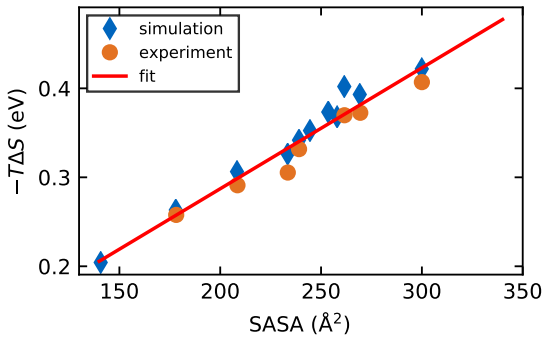


Figure S7: Solvent accessible surface area (SASA) against hydration entropy $-T\Delta S$ for alkanes in water. The experimental (orange circles) and simulated (blue diamonds) data points are adapted from 10. The red line presents a linear fit to all data points.

oxides, and sulfides have been shown to yield similar hydration entropies.[11]

Table S11: Maximum values of the change in solvent accessible surface area (ΔSASA) and corresponding hydration free entropy $-T\Delta S$ following the relation for alkanes[10] (see text).

| | ΔSASA (Å$^2$) | $-T\Delta S$ (eV) |
|---|---|---|
| | Cu(211) | |
| CO | 19.04 | 0.03 |
| CHO | 20.88 | 0.04 |
| COH | 4.74 | 0.01 |
| OCCHO | 36.85 | 0.06 |
| OH | 6.72 | 0.02 |
| | Cu(111) | |
| CO | 15.23 | 0.03 |
| OH | 7.27 | 0.02 |
| | Au(111) | |
| CO | 17.43 | 0.03 |
| OH | 7.92 | 0.02 |
| OOH | 16.93 | 0.03 |
| | Pt(111) | |
| CO | 11.35 | 0.02 |
| OH | 6.59 | 0.02 |
| OOH | 12.99 | 0.025 |

We determine the change of the SASA for the adsorbates in our test set via the solvation cavities in our implicit solvent simulations. In general, the SASA varies slightly based on the adsorption site. For a conservative estimate, we consider the maximum values of the

change in the SASA which are listed in Tab. S11. For small adsorbates like *CO and *OH, the change in the SASA is in the order of 10-20 Å and for the larger *OCCHO around 40 Å. From the fitted relation to the hydration entropy (c.f. Fig. S7) we find hydration entropies to be about 10-60 meV.

The estimated values of the hydration entropy are in all cases below the uncertainty of our AIMD results. A comparison of the solvation free energies from implicit solvation to internal solvation energies from AIMD is thus justified for our test set.

# VII Size effects in AIMD simulations

The thickness of the water film included in our model of the metal/water interface is less extended in comparison to previous studies.[12,13] While our smaller simulation setup is computationally feasible for the treatment of many adsorbate/surface combinations, it is not necessarily clear whether size effects may impede results. For this reason, we evaluate the effect of the water layer thickness and show that size effects are minor and – if at all – affect energetics based on small changes of the interface. This ultimately implies that the solvent interactions are highly local and there is no influence of the solvent bulk.

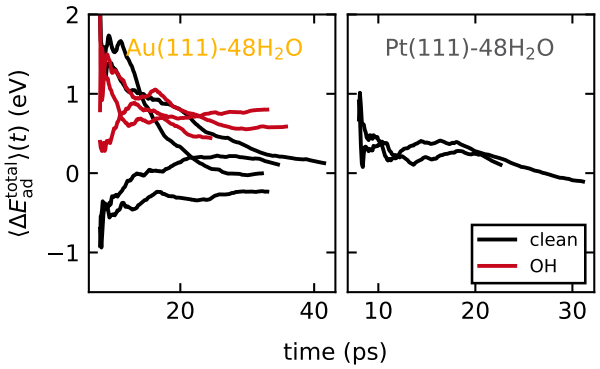


Figure S8: Total average adsorption energy (eq. 1 main text) against simulation time $\langle \Delta E_{ad}^{total} \rangle (t)$ (cumulative average) after the equilibration period of 8 ps for all individual trajectories of the extended Au(111) and Pt(111) systems (see text). The gas phase references are kept constant for all time steps.

The water thickness is quantitatively evaluated for the Au(111) surface. This surface

shows a particularly low water density in its "bulk" segment with $\geq 0.85$ of the experimental water density ($\rho_{\text{exp}}$) when using 3 water "layers" (24 $H_2O$ molecules) in comparison to the other water/metal interfaces. A most dramatic effect of the water layer thickness can therefore be expected for this metal/water interface. We extend the Au(111) system to include 6 water "layers" (48 $H_2O$ molecules) while maintaining all other simulation parameters. We investigate the clean and *OH covered Au(111) surface. For each system, we evaluate 4 and 3 individual trajectories of at at least 30 ps, respectively. The large systems converge considerably slower. For this reason, we commence data sampling after 8 ps (compare Fig. S1 and S8). As shown in Fig. S8, the overall equilibration is of worse quality than for the non-extended Au(111) systems with half of the trajectories having a remaining total energy drift $\leq 60$ meV. Therefore, quantitative results may be less reliable.

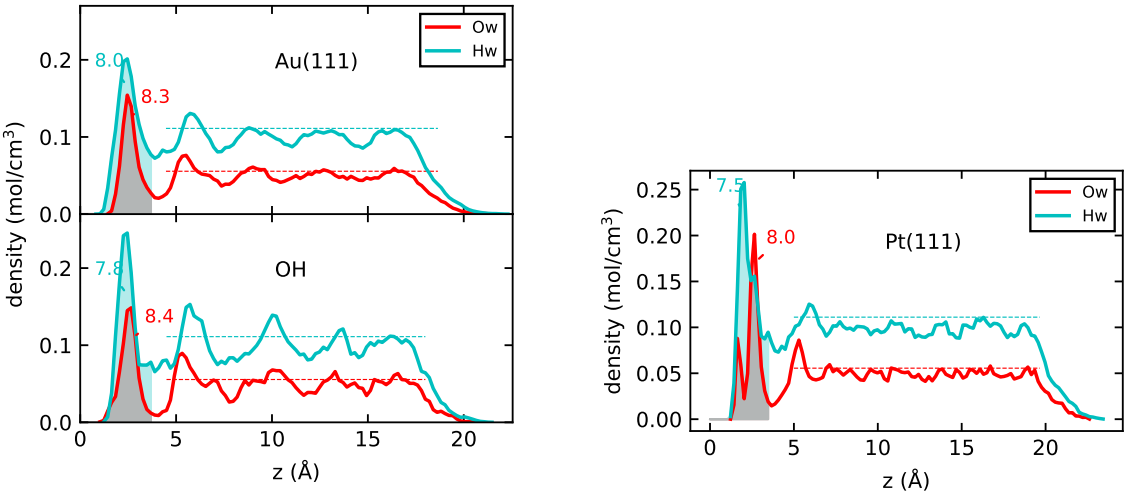


Figure S9: Average atomic densities along the surface normal $z$ of the extended Au(111) system (left) and Pt(111) system (right) with 48 $H_2O$ molecules (i.e. 6 water "layers"). The densities for the clean and *OH covered Au(111) surface are depicted in the top and bottom panels. The atomic density of O ($O_w$) and H ($H_w$) from water are shown in red and cyan, respectively. The experimental atomic densities of bulk water are depicted by the dotted lines. The shaded area corresponds to the integrated area of the first water layer with the numeric values included, normalized to $H_2O$ molecules per unit cell.

Employing six water "layers" leads to virtually no change in the average workfunction with 4.81 eV $\pm$ 0.08 against 4.89 $\pm$ 0.1 eV for three water "layers". This indicates that

the water/vacuum interface appears insensitive of the here compared water film thicknesses. Otherwise, the metal/water interface slightly changes due to the increase in thickness of the water film. With 48 $H_2O$ molecules, the density of the "bulk" segment reaches 1.0 instead of 0.85 of $\rho_{\text{exp}}$ (see Fig. S9). As a consequence, the average number of adsorbed water molecules ($\langle n_{\text{ad}}^{\text{H}_2\text{O}} \rangle$) increases from 0.07 to 0.38 for the clean surface. The absolute $\langle n_{\text{ad}}^{\text{H}_2\text{O}} \rangle$ resulting from this increase is still small as compared to the other metal/water interfaces (compare Fig. 6 in main text). In the presence of an *OH adsorbate the water adsorption only changes slightly from 1.04 to 0.90 whereby both values have a high uncertainty (c.f. Fig. S4). In contrast to the water adsorption, the average number of hydrogen bonds to *OH is nearly unaffected with 2.95 vs. 2.96. The resulting adsorption energy of *OH is $0.69 \pm 0.12\,\text{eV}$ which is moderately increased compared to the three water "layer" value of $0.53 \pm 0.08\,\text{eV}$. A therein following decrease of the solvation energy by 0.14 eV is likely due to the increase in competitive water adsorption. In fact, the associated shift of $\Delta\langle n_{\text{ad}}^{\text{H}_2\text{O}} \rangle$ approximately matches the energetic shift in the solvation energy. We note that we only expect such a size-effect for Au(111) in our test set since the other metal surfaces exhibit a water density $\rho_{\text{exp}}$ of $\geq 0.95$. We confirm the convergence of the metal/water interface for the three water "layer" system for the clean Pt(111) surface by comparing to AIMD simulations employing six water "layers". These (less converged) AIMD simulations (c.f. Fig. S8) exhibit a water density in the "bulk" segment of 0.99 $\rho_{\text{exp}}$ (see Fig. S9) and a virtually unchanged $\langle n_{\text{ad}}^{\text{H}_2\text{O}} \rangle$ of 1.78 against 1.83 for the three water "layer" system (c.f. Sec. IV). Further, we cannot find any other "hidden" effects stemming from the considerably larger water bulk since all changes of the solvation energy of *OH on Au(111) can be related to changes of the metal/water interface. This observation is in line with previous findings.[14]

# VIII Size effects in metal slabs

## VIIIa Artifact from the slab thickness of Pt(111)

We found a DFT artifact in our Pt(111) slab models. In this artifact a local minimum emerges where the top layer of the Pt(111) metal slab shifts orthogonal to the surface normal as depicted in Fig. S10. In this configuration, the unconstrained surface layer is top-top coordinated towards the lower lying metal layer breaking the fcc-packing. This artifact is only found for the Pt(111) slabs and disappears for thicker slab models (i.e. $> 3$ layers). It is thereby not dependent on the positional constraint of the lower metal layers but only on the number of metal layers employed.

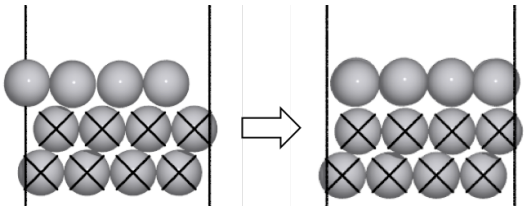

Figure S10: Artifact encountered in a 3 layer metal slab of Pt(111). The shift of the top layer from the fcc configuration (left) to the top-top coordination (right) appears as an artifact in the here used RPBE-D3 setup.

We observed the erroneous metal layer configuration only in two trajectories of the *OOH adsorbate on Pt(111). Once the system arrived at the artificial local minimum, we excluded the remainder of the trajectory (dashed lines in Fig. S1). This accounts for 10 and 20 ps in two *OOH trajectories (labelled # 3 and # 4 in Tab. S1).

## VIIIb Symmetric vs. non-symmetric slabs

In this work adsorption energies at 0 K are computed through geometry optimizations of symmetric slab models (adsorbates on both sides of the slab). This setup allows to determine the workfunction when using continuum solvation and ultimately gives potential control for grand canonical DFT simulations.[15] We compare these to adsorption energies of AIMD simulations using a non-symmetric slab (adsorbates only on one side of the slab). To evaluate

a possible error based on these two slab models, we benchmark adsorption energies of *CO on all employed metal slabs. As shown in Fig. S11, the adsorption energies are in most cases consistent. Deviation is found for Pt(111) with the symmetric slab setup having $<$ 0.05-0.1 eV less stable adsorption energies. A deviation is also found for *CO on the top sites of the Au(111) with the symmetric slab setup having more stable adsorption energies by $<$ 0.07 eV. These values explain in part the few observed deviations between the differences of adsorption and solvation energies between continuum solvation and AIMD (c.f. Fig. 9 in the main text). Notably the deviations are however consistent with and without continuum solvation and therefore do not affect solvation energies which are central in this study.

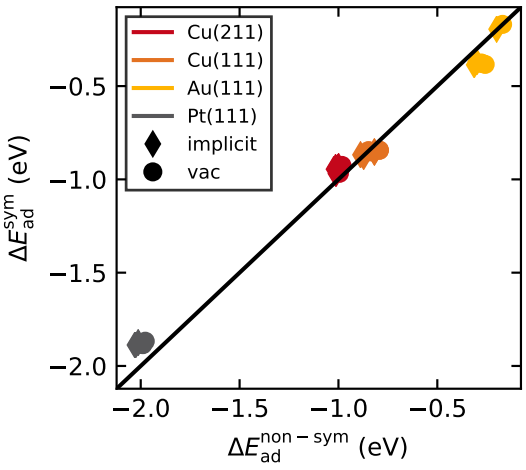


Figure S11: Parity plot of the adsorption energies of *CO on Cu(211), Cu(111), Au(111), and Pt(111) calculated with a symmetric and non-symmetric slab model. Diamonds represent adsorption energies with a continuum solvation model (implicit) and circles adsorption energies without (vac).

# References

(1) Gunceler, D.; Letchworth-Weaver, K.; Sundararaman, R.; Schwarz, K. A.; Arias, T. The importance of nonlinear fluid response in joint density-functional theory studies of battery systems. *Modelling Simul. Mater. Sci. Eng.* **2013**, *21*, 074005.

(2) Mathew, K.; Hennig, R. G. Implicit self-consistent description of electrolyte in plane-wave density-functional theory. *arXiv preprint* **2016**,

(3) Giannozzi, P. et al. QUANTUM ESPRESSO: a modular and open-source software project for quantum simulations of materials. *J. Phys. Condens. Matter* **2009**, *21*, 395502.

(4) Andreussi, O.; Dabo, I.; Marzari, N. Revised self-consistent continuum solvation in electronic-structure calculations. *J. Chem. Phys.* **2012**, *136*.

(5) Hammer, B.; Hansen, L. B.; Nørskov, J. K. Improved adsorption energetics within density-functional theory using revised Perdew-Burke-Ernzerhof functionals. *Phys. Rev. B* **1999**, *59*, 7413.

(6) Grimme, S.; Antony, J.; Ehrlich, S.; Krieg, H. A consistent and accurate ab initio parametrization of density functional dispersion correction (DFT-D) for the 94 elements H-Pu. *J. Chem. Phys.* **2010**, *132*, 154104.

(7) Grimme, S. Density functional theory with London dispersion corrections. *Wiley Interdiscip. Rev.: Comput. Mol. Sci.* **2011**, *1*, 211–228.

(8) Abild-Pedersen, F.; Greeley, J.; Studt, F.; Rossmeisl, J.; Munter, T.; Moses, P. G.; Skulason, E.; Bligaard, T.; Nørskov, J. K. Scaling properties of adsorption energies for hydrogen-containing molecules on transition-metal surfaces. *Phys. Rev. Lett.* **2007**, *99*, 016105.

(9) Tripković, V.; Skúlason, E.; Siahrostami, S.; Nørskov, J. K.; Rossmeisl, J. The oxygen reduction reaction mechanism on Pt(111) from density functional theory calculations. *Electrochimica Acta* **2010**, *55*, 7975 – 7981.

(10) Gallicchio, E.; Kubo, M.; Levy, R. M. Enthalpy- entropy and cavity decomposition

of alkane hydration free energies: numerical results and implications for theories of hydrophobic solvation. *J. Phys. Chem. B* **2000**, *104*, 6271–6285.

(11) Kubo, M. M.; Gallicchio, E.; Levy, R. M. Thermodynamic decomposition of hydration free energies by computer simulation: Application to amines, oxides, and sulfides. *J. Phys. Chem. B* **1997**, *101*, 10527–10534.

(12) Sakong, S.; Forster-Tonigold, K.; Axel, G. The structure of water at a Pt(111) electrode and the potential of zero charge studied from first principles. *J. Chem. Phys.* **2016**, *144*, 194701.

(13) Sakong, S.; Axel, G. The electric double layer at metal-water interfaces revisited based on a charge polarization scheme. *J. Chem. Phys.* **2018**, *149*, 084705.

(14) Natarajan, S. K.; Behler, J. Neural network molecular dynamics simulations of solid–liquid interfaces: water at low-index copper surfaces. *Phys. Chem. Chem. Phys.* **2016**, *18*, 28704–28725.

(15) Nattino, F.; Truscott, M.; Marzari, N.; Andreussi, O. Continuum models of the electrochemical diffuse layer in electronic-structure calculations. *J. Chem. Phys.* **2019**, *150*, 041722.